Additional Information: This is an Author Accepted Manuscript of an article published in Advanced Energy Materials.

An Active Oxygen Evolution Electrocatalyst Motif Created by Confining Transition Metal Cations within Layered Structures

Joel Sanchez,[1,2,3] Michaela Burke Stevens,[1,2,3] Alexandra R. Young,[1] Alessandro A. Gallo,[2,3]

Meng Zhao,[3] Mario V. Ramos-Garcés,[4] Jorge L. Colón,[4] Laurie A. King,[5] Michal Bajdich,[3] and

Thomas F. Jaramillo[1,2,3]

[1]Department of Chemical Engineering, Stanford University, Stanford, CA 94035, USA

[2]SUNCAT Center for Interface Science and Catalysis, Stanford University, Stanford, CA 94035, USA

[3]SUNCAT Center for Interface Science and Catalysis, SLAC National Accelerator Laboratory, 2575 Sand Hill Road, Menlo Park, CA 94025, USA

[4]Department of Chemistry, University of Puerto Rico at Río Piedras, San Juan, PR 00925, USA

[5]Faculty of Science and Engineering, Manchester Metropolitan University, Manchester, M1 5GD, UK

Corresponding Authors: Laurie A. King (l.king@mmu.ac.uk), theory corresponding author Michal Bajdich (bajdich@slac.stanford.edu), and Thomas F. Jaramillo (jaramillo@stanford.edu)

Abstract

Unique classes of active-site motifs are needed to redefine and improve electrocatalysis. Herein we have engineered a new catalyst motif for the oxygen evolution reaction (OER) consisting of nickel-iron transition metal cations confined within a layered zirconium phosphate matrix. We find that with optimal intercalation, confined Ni/Fe catalysts have an order of

26 magnitude improved mass activity compared to more conventional surface-adsorbed systems in
27 0.1 M KOH. Interestingly, the confined environments within the layered structure also stabilizes
28 Fe-rich compositions (90%) that are difficult to study in more traditional formats. By grafting inert
29 molecules to the outer surface we have evidence that the intercalated Ni/Fe cations stay within the
30 interlayer during catalysis and serve as the active site. After determining a possible structure
31 (wycherproofite), density theory was shown to correlate with the observed experimental
32 compositional trends. We further identify that the improved activity of this motif is correlated to
33 the Fe and water content/composition within the confined space. This work highlights the catalytic
34 enhancement possibilities available through confined active-site motifs, thus opening new avenues
35 to develop classes of improved catalysts within unique nanoscale chemical environments.

36 **TOC Image**
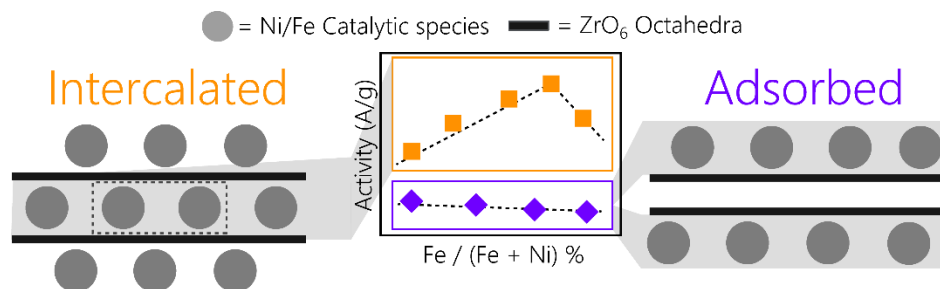
37 **Introduction**

38   The oxygen evolution reaction (OER) plays a key role in many emerging energy
39 conversion technologies including but not limited to water electrolysis,[1] metal-air batteries,[2] and
40 CO_2 electorlysis.[3] The use of alkaline electrolytes enables the use of non-precious metal catalysts
41 such as *3d*-transition metal oxides[4,5], (oxy)-hydroxides[5], layered double hydroxides[6], metal
42 organic frameworks (MOF)[7], and single-atom systems[8]. In particular, the doping of Fe into
43 inactive Ni (oxy)hydroxide (Ni(OH)$_2$/NiOOH) materials has yielded high performing catalysts
44 with long term durability.[5,9–14] Various promising routes have focused on increasing activity of
45 these catalyst systems by methods that increase the number of active sites or increase the intrinsic
46 activity of each site. While the former has been employed extensively in the literature, the latter
47 has been difficult to ascertain. Herein, we create a new catalyst motif, breaking away from
48 conventional surface based OER catalysts in the hopes of overcoming the bottlenecks that have

49   hindered conventional catalyst systems for decades. This new motif involves confining Ni and Fe

50   catalysts species within the θ phase of zirconium phosphate ($Zr(HPO_4)_2 \cdot 6H_2O$, a highly hydrated

51   derivative of the more widely used $Zr(HPO_4)_2 \cdot H_2O$, α-zirconium phosphate).

52   Strategies such as the encapsulation or confinement of active species within layered

53   materials have recently emerged in computational and experimental work as promising routes to

54   enhanced activity.[15] Such strategies confine the active sites, influencing the reaction intermediates

55   by providing microenvironments or solvation structures that have a significant effect on catalytic

56   performance.[16–22] The act of catalyst confinement can potentially create unique active site

57   environments that are not accessible by traditional surface-based motifs. Density functional theory

58   (DFT) calculations have highlighted layered materials as a promising platform for breaking OER

59   scaling relationships by providing a planar channel that has a unique microenvironment that

60   enables new types of adsorbate-catalyst interactions.[23,24] Experimental work has shown that the

61   confinement of active species within birnessite,[25–28] MoS_2,[29,30] and graphene[16,31,32] improve the

62   activity, stability, and selectivity, respectively, of electrochemical reactions. With the increasing

63   number of confined catalytic platforms, it is possible to build a template to provide experimental

64   evidence showcasing the nature of active species within a confined space. Furthermore, in

65   exploring confined environments, several effects are of interest that alter the chemical nature of

66   the confined platform, including but not limited to interlayer spacing, interlayer solvation

67   dynamics, and co-intercalated species. Understanding how these factors govern performance and

68   elucidating if confined catalytic species are active motivates further study.

69   Of the numerous layered materials of interest for exploring confined environments, θ-

70   zirconium phosphate ($Zr(HPO_4)_2 \cdot 6H_2O$) is one promising candidate that has shown impressive

71   property and application tunability as a function of ion intercalation for a wide range of

72   technologies including biosensors, [33–35] vapochromic materials,[36–38] and drug delivery.[39–43]

73   However, for electrocatalysis, while layered and nanostructured (sheets, cubes, rods, and spheres)

74   zirconium phosphate morphologies have shown promise as transition metal oxide supports, no

75   intrinsic performance enhancements from confinement have previously been observed.[44–47]

76   Extracting the factors that govern the enhancements in the nanoscopic channels could help the

77   development of strategies and further the advancement of confined catalyst systems. [44–47]

78   In this work, zirconium phosphate is used as a platform to achieve OER catalysis within
79   confined environments, where a definitive interlayer spacing provides for catalysts to be developed
80   with high activity and stability. We show that the intercalation of Ni and Fe cations within θ-
81   zirconium phosphate modulates the homogeneity of the interlayer spacing as a function of cation
82   loading and produces three distinct intercalated phases. Fully intercalated systems are shown to
83   have an improved intrinsic activity when normalized to their mass, in relation to adsorbed
84   counterparts, and an optimum is revealed for an Fe-rich intercalated (I-$Ni_{0.1}Fe_{0.9}$) catalyst,
85   particularly interesting as Fe-rich catalysts are not viewed as optimum in more conventional
86   catalyst formats. By means of studies coupling XRD, ICP-MS, and chronopotentiometry, we
87   verify that the catalytic species confined within the interlayer are stable. Using octadecyl
88   isocyanate (ODI) to displace surface bound (adsorbed) Ni/Fe species from I-$Ni_{0.1}Fe_{0.9}$ catalyst, we
89   demonstrate that the majority of the OER activity originates from Ni/Fe species intercalated within
90   the structure, rather than at the outer surface. Computationally, we explore a number of intercalated
91   structures for their stability and activity and identify phosphate groups as the main anchoring sites.
92   The confined environment provided by zirconium phosphate improves activity (on both a
93   geometric and mass basis), effects arising from various factors, including perturbations to the water
94   environment within the confined interlayer as well as the tunability of the cation composition that
95   changes the nature of the active site. This work shows the promise of layered materials with
96   phosphate groups as an emerging platform to confine catalytic species, leading to physical and
97   chemical effects that can be leveraged for increased performance for a variety of chemical
98   reactions.

99   **Results and Discussion:**

100   **Adsorbed and Intercalated Zirconium Phosphate Structures**

101   α-Zirconium phosphate (**Figure 1A**) is a non-precious-metal layered material that consists
102   of zirconium atoms octahedrally coordinated with oxygen atoms of bridging phosphate groups.
103   The three oxygens of each phosphate group bridge three different zirconium atoms in a corner-
104   sharing fashion. The fourth and non-bridging oxygen of each phosphate group is bonded to an
105   acidic exchangeable proton. Ion-exchange of this proton, located above and within the layers with
106   other cation species enables the modification of the surface acidity, hydrophobicity/hydrophilicity,

4

107 textural properties, and changes in interlayer spacing making zirconium phosphate highly versatile

108 and useful for numerous applications.[48] The layer spacing can also be controlled simply by

109 changing the number of interlayer waters between the sheets. The α- and θ-$Zr(HPO_4)_2 \cdot nH_2O$

110 phases (**Figure 1B**, with n=1 and n=6 for the α and θ phases, respectively) have been the most

111 highly studied polymorphs and their interlayer distances are 7.6 Å and 10.4 Å, respectively.[49]

112 When intercalated with different ions, structural changes have been observed for intercalated

113 derivatives of zirconium phosphate and these changes disrupt the standard orientation of the

114 phosphate groups and interlayer spacings. [50,51]

115 It is known that the α- phase's interlayer distance of 7.6 Å is too small to intercalate cation

116 species with a ionic diameter larger than 2.61 Å without additional techniques such as solvent

117 exchange, sonication, heating, or additional energy into the system to overcome the intercalation

118 threshold barrier.[33,42,43,52] The θ-phase, on the other hand, with an interlayer distance of 10.4 Å

119 (due to six interlayer water molecules per formula unit) readily allows for the direct intercalation

120 of larger positively charged species. In this work, we utilize the α- and θ- zirconium phosphate

121 phases to strategically synthesize surfaced adsorbed (Phase 0, using the α-phase) and interlayer

122 intercalated

5
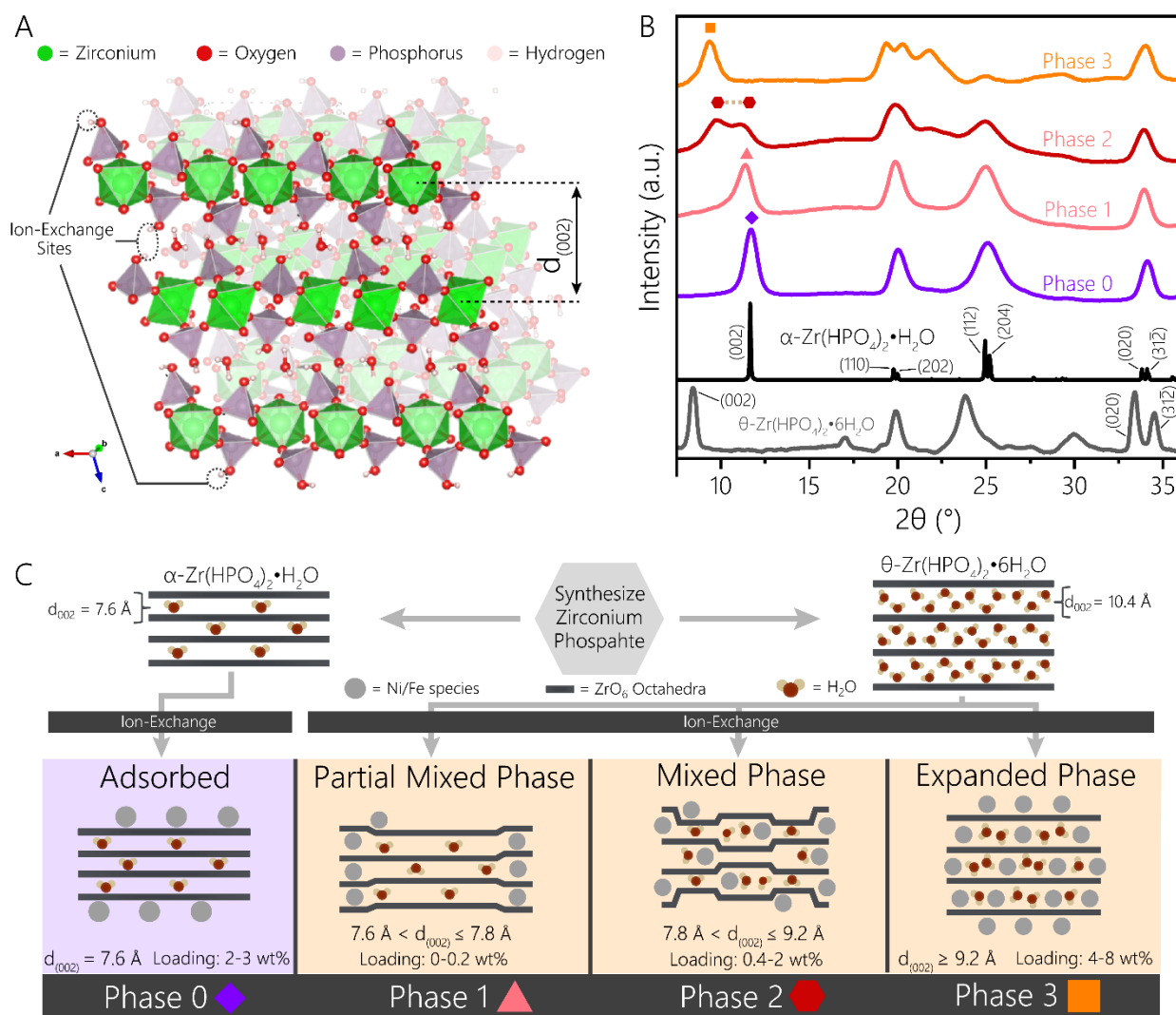
Figure 1 – (A) Crystal structure of α-zirconium phosphate (ICSD 1281) where ZrO_6 octahedra (green) are linked to phosphate tetrahedra (gray). Interlayer distance for the (002) reflection is characterized by the distance between Zr atoms in opposite layers and is altered by the amount of interlayer water and/or intercalated species. Ion-exchange of cations occurs at the exchangeable protons (dashed circles) found within the interlayer and on the outer surfaces of the zirconium phosphate nanoparticles. In this schematic, only a select few protons are encircled whereas the sites of ion exchange occur throughout the layered material. (B) Representative X-ray diffraction patterns of the α-phase (ICSD 1281), the experimentally collected θ-phase, and the four synthesized phases at a Fe/(Fe+Ni) composition of ~90%. (C) Schematic illustration of the synthesis process for intercalated and adsorbed zirconium phosphate systems. Purple and orange backgrounds correspond to the α-phase and the θ-phase undergoing ion-exchange to form adsorbed and intercalated Ni/Fe catalyst systems, respectively. Four different systems are produced from two zirconium phosphate phases, α- and θ-zirconium phosphate, and are subdivided into adsorbed (Phase 0) and intercalated (Phage 1-3) systems, respectively. For intercalated systems, the three different phases correspond to the different mixing of θ-zirconium phosphate as a function of increasing cation (Ni + Fe) loading (relative to total catalyst loading). Dark gray lines represent the (002) planes of zirconium phosphate where the interlayer distance (d_{002}) ranges from 7.6 to 10.4 Å)

123

6

124 catalysts (Phases 1-3, using the θ-phase) with a range of Ni/Fe compositions. To synthesize this

125 broad set of catalysts, we systematically vary cation loading by modifying the concentration and

126 molar ratio of the metal salt precursors relative to the zirconium phosphate host material. We

127 employ X-ray diffraction (XRD) to observe the extent of intercalation, compared to the control α-

128 and θ- phases, by tracking the lowest angle (002) peak (**Figure 1B**). A schematic of the different

129 phases synthesized is depicted in **Figure 1C**. Furthermore, transmission electron microscopy

130 (TEM) micrographs showcase no distinct morphological differences between the four systems

131 (**Figure S1**). Catalysts with various Ni/Fe ratios adsorbed to the surface are synthesized using α-

132 zirconium phosphate as a starting material (**Figure 1C**, Phase 0). The absence of intercalation is

133 confirmed through XRD (**Figure 1B**) which shows a pattern consistent with an α-zirconium

134 phosphate that has an interlayer distance of 7.6 Å. As described above, the Ni and Fe cations are

135 unable to diffuse within the layers and thus, the ion-exchange of cations occurs only on the

136 bridging phosphate groups of the outermost surface of the nanoparticles.

137 Co-intercalated catalysts are synthesized from the θ-zirconium phosphate precursor. In

138 these syntheses, the Fe and Ni ions can adsorb both onto the surface of the material as well as

139 intercalate into the θ-zirconium phosphate structure (**Figure 1C**, Phase 1-3 (P-1, P-2, and P-3)).

140 By modulating the total Ni/Fe cation loading during the ion-exchange process, while keeping the

141 amount of θ-zirconium phosphate constant, we synthesize three unique phase mixtures of

142 intercalated Ni/Fe zirconium phosphate that vary by the degree of interlayer expansion. Degree of

143 expansion is characterized by a shift in the (002) peak or by the appearance of multiple peaks at

144 2θ values lower than 11.5°. Based on previous reports, at low loadings, the introduction of cation

145 and water species occurs initially at the edges of the zirconium phosphate sheets by the removal

146 or partial removal of the solvation shell of a positively charged species.[53] Once removed, the

147 intercalating species can enter through the edges of the zirconium phosphate layers (P-1) causing

148 an expansion of the edges. Specifically, P-1 systems shows expansion of up to 0.2 Å compared to

149 the parent α-zirconium phosphate phase. This slight expansion, observed concurrently with the

150 broadening of the (002) peak, indicates that species are introduced to the outermost galleys of the

151 zirconium phosphate sheets thus expanding the edges of the interlayer.[53] At intermediate loadings,

152 diffusion of the positively charged species is hypothesized to occur from the edges towards the

153 center of the galleries (P-2). As seen in the diffractograms, the layered structure in the P-2 systems

is highly perturbed showcasing two distinct peaks between 7.8 and 9.2 Å – one at approximately $2\theta \approx 11.5°$ and another at lower 2θ values (9.5-9.8°) indicating that a mixed phase with partial (P-1) and near full layer expansion (P-3) is present. The left most peak is indicative of a new intercalated phase that is not yet fully expanded while the right most peak is representative of the parent α-zirconium phosphate structure with slight expansion. Finally, at high loadings, the insertion of additional species is expected to manifest in the formation of new bonds that drives the diffusion of cations to move further into the channels until the layers of the zirconium phosphate are fully expanded (P-3). Indeed, P-3 systems display a shift of the 002 peak to lower 2θ values (9.4-9.6°) and no peak at ~7.6 Å, as expected for a pure fully expanded intercalated phase material. Characteristic diffractograms for all phases are shown in **Figure S2** as a function of increasing Ni/Fe content and are shown to exhibit similar diffractograms as described above. The confirmation of various distinct phases of Ni/Fe zirconium phosphate systems through XRD enables the assessment of composition, structure, interlayer distance, and loading on performance for the OER.

Structure, Conductivity, and Activity for Ni/Fe-modified Zirconium Phosphate Catalysts: Ni/Fe Adsorbed on the Surface and/or Intercalated Within the Layers

To probe electrochemical OER activity as a function of Ni:Fe composition and confinement, the prepared suite of adsorbed (P-0) and intercalated (P-1, P-2 and P-3) catalysts were evaluated using cyclic voltammetry. Towards rationalizing observed activity trends, we evaluated the as-prepared interlayer spacing, conductivity, and OER performance assessed through the overpotential for the OER at 10 mA cm^{-2} (η_{10}) and mass activity at an overpotential of 350 mV (M.A.$_{350}$) for a large Fe:Ni compositional range (**Figure 2**). Both performance metrics are from the average of a forward and reverse sweep (1st cycle) of the voltammograms (10 mV s^{-1}) in 0.1 M KOH. **Table S1** details all the values depicted in **Figure 2**.

As described in detail previously, the interlayer distance varies with the extent of Ni/Fe cation intercalation to create four unique phases. The various phases were accessed by modulating either the starting layered structure (P-0 vs P-1−P-3) or cation loading (P-1−P-3). **Figure 2A** (full diffractograms are shown in Figure S1A-D) shows the interlayer spacing as function of the Ni:Fe ratio. For each phase, we see minimal changes in interlayer distance across the compositional ranges indicating that interlayer spacing is not composition dependent. This allows for the comparison of activity within each phase across compositions without the influence of a variable interlayer distance. **Figure 2B** displays the four-point probe conductivity measurements assessed for the catalysts powders (prior to electrochemistry) as a pressed pellet. **Figure 2B** shows that as the Fe content increases from 0 to 100%, all catalyst systems show a noticeable decrease in conductivity by 1-2 orders of magnitude. Nearly all systems show reduced catalyst conductivity as a function increased Fe content, both absolute or measured relative to Ni and Fe wt% (**Figure S3A**) as compared to α-zirconium phosphate (black dashed line). Based on previous in situ conductivity reports, we hypothesize that the Fe content readily converts to iron oxide species leading to a more insulating catalyst.[54]
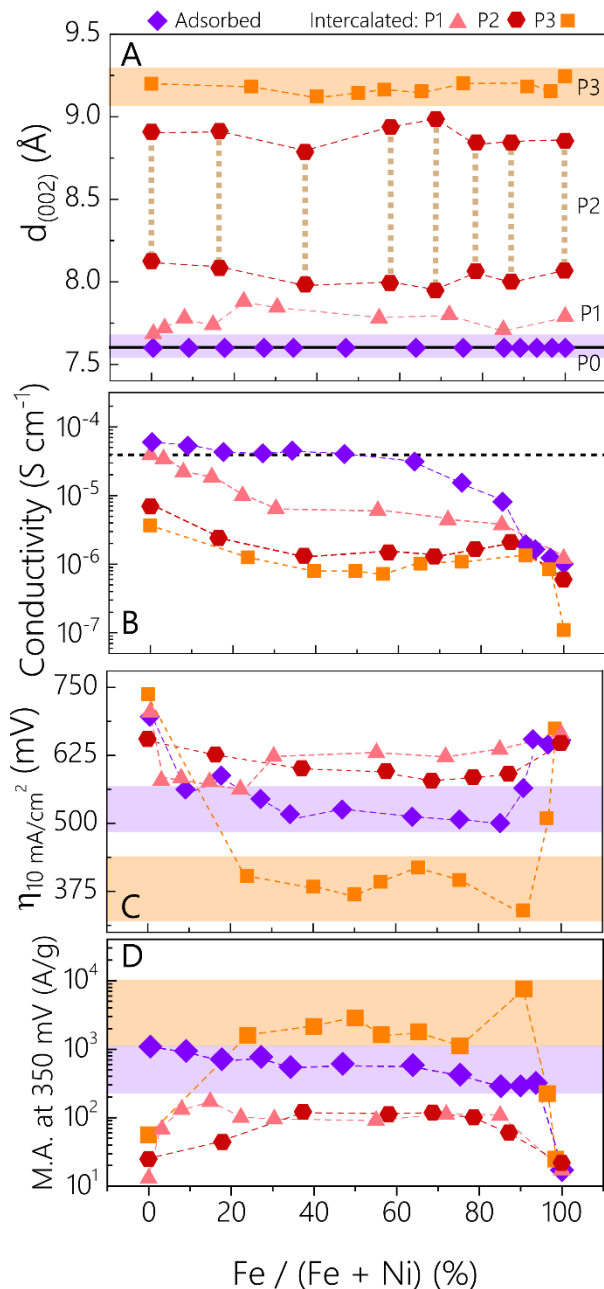
Figure 2 - Ni-Fe compositional dependence on **(A)** interlayer distance obtained for the (002) plane of zirconium phosphate from XRD measurements. Solid black line represents the interlayer spacing of α-zirconium phosphate. **(B)** Four-point probe conductivity measurements. Black dashed line represents the four-point probe conductivity of α-zirconium phosphate. **(C)** overpotential for the OER (relative to 1.23 V vs. RHE) at 10 mA cm^{-2} in 0.1 M KOH, and **(D)** mass activity at 350 mV for adsorbed (purple diamonds) and intercalated (P-1: salmon triangles, P-2: red hexagons, P-3: orange squares) Ni/Fe zirconium phosphate catalysts. Purple and orange and highlighted regions emphasize

9

207   To understand the role of activity enhancement as a function of spacing, we compared

208   η_{10} (**Figure 2C**) and M.A.$_{350}$ (**Figure 2D**) at all Ni/Fe ratios and phases. Specifically, η_{10} assesses

209   activity on a geometric basis, which can be dependent on catalyst loading, while M.A.$_{350}$ provides

210   an intrinsic activity assessment by normalizing to the total cation mass obtained from ICP-MS.

211   The M.A.$_{350}$ is particularly important since improved activity can be correlated with an increased

212   loading of Ni and Fe species within P1- P-3 systems with P-3 systems having the highest Ni/Fe

213   loading **(Figure S3B)**. It is important to note that the M.A. is also likely an underestimation of

214   activity as it assumes that all Ni/Fe cations are active. By both metrics, consistent with previous

215   experimental reports, all systems, on average, have enhanced mixed Ni/Fe performance in relation

216   to the elevated η_{10} and reduced M.A.$_{350}$ for monometallic systems.[44-47]

217   For adsorbed (P-0) systems, pure Ni and Fe compositions exhibit high η_{10} of 695 and 592

218   mV and M.A.$_{350}$ values of 1025 and 120 A/g, respectively. As the amount of Fe content relative to

219   Ni increases (0 to 9 %), there is an initial improvement of ~ 130 mV. Increasing the Fe ratio up to

220   85% further reduces the overpotential to a minimum ~ 500 mV. However, once the Fe content

221   surpasses 90%, η_{10} is negatively impacted as observed by the η_{10} = 592 mV at 100 % Fe content.

222   Furthermore, when assessed for M.A.$_{350}$, P-0 systems exhibits a two orders of magnitude reduction

223   in M.A$_{350}$ (1088-12 A/g) from 0 to 100% Fe content relative to Ni. For intercalated systems,

224   improved η_{10} based on Ni/Fe synergism are observed for Ni/Fe P-1 (low-loading) and P-2

225   (intermediate-loading) systems. However, compared to the adsorbed system, both P-1/P-2

226   systems, on average, have worse performance than P-0 by ~50 mV and ~600 A/g on a M.A.$_{350}$

227   basis. Coincidentally, P-1 and P-2 also have an order of magnitude lower conductivity than the

228   adsorbed (P-0) systems which could indicate that their poor performance is due to inhibited

229   electron transfer through the zirconium phosphate sheets. In contrast, the high-loading fully

230   expanded systems (P-3), show improved η_{10} by an average of ~ 100 mV and ~ 150 mV compared

231   to adsorbed (P0) and P-1/2 systems, respectively at all mixed Ni/Fe compositions. In terms of

232   M.A.$_{350}$, P-3 systems, on average, are ~3 times more active on a mass basis compared to adsorbed

233   systems (~ 2400 vs. ~ 740 A/g, respectively) at similar compositions and are an order of magnitude

234   more active than P-1/2 systems (~ 2400 vs. ~110 A/g, respectively). This analysis indicates that

235   among all the unique interlayer environments made possible from the different phases synthesized

236 (P-1−P-3), the most active catalysts involved interlayer spacings characteristic of the P-3 systems
237 with intercalated, mixed Ni/Fe cations of a high Fe content.

238 Computational studies have indicated that an optimal interlayer spacing can favorably
239 impact metal-adsorbate binding energies and enhance activity.[23] We hypothesize that the interplay
240 between the optimal interlayer spacing and Ni/Fe composition in the P-3 systems may be
241 responsible for the improved performance relative to the adsorbed systems. An improvement in
242 activity is not universally observed for confined metal species within zirconium phosphate at a
243 similar interlayer spacings and loadings when compared to adsorbed counterparts.[44] This
244 nonuniversal trend indicates that the active site environment and cation composition in confined
245 (P-3) mixed Ni/Fe compositions (**Figure S3C**) is unique. To further investigate this observed
246 phenomenon, we examine the differences between the most active intercalated composition (P-3,
247 90% Fe content relative to Ni, $\eta_{10} = 340\ mV$) and its adsorbed (P-0, $\eta_{10} = 655\ mV$)
248 counterpart.

249 **Elucidating Surface versus Confined Catalysis: An Activity and Stability Assessment for**
250 **Adsorbed and Intercalated Ni$_{0.1}$Fe$_{0.9}$ Catalyst Systems**

251 ***Majority of Ni/Fe Species Remain within the Zirconium Phosphate Layers during***
252 ***Catalysis***.

253 Before probing the root of the intercalated enhancement, we first assessed the material
254 stability and the longevity of the Ni/Fe species during catalysis either within the layers or adsorbed
255 on the surface (**Figure 3**). As clarified previously, fully expanded P-3 intercalated catalysts
256 outperform adsorbed P-0 catalysts for all mixed Ni/Fe compositions. Interestingly, we see that the
257 most active intercalated P-3 compositions range between 28 – 90 % Fe with a maximum at 90 %
258 Fe, labeled as I-Ni$_{0.1}$Fe$_{0.9}$, P-3 in **Figure 3A**. Due to its enhanced activity and high Fe content, we
259 focus on this composition for our in-depth stability and intrinsic activity. To assess the change in
260 metal loading, the amount of catalyst that is responsible for the OER current, and gauge the
261 integrity of the layers during catalysis, I-Ni$_{0.1}$Fe$_{0.9}$ intercalated (P-3) and adsorbed (A-Ni$_{0.1}$Fe$_{0.9}$,
262 P0) systems were monitored after cyclic voltammetry, by ICP-MS and XRD, respectively (**Figure**
263 **3A-C**).
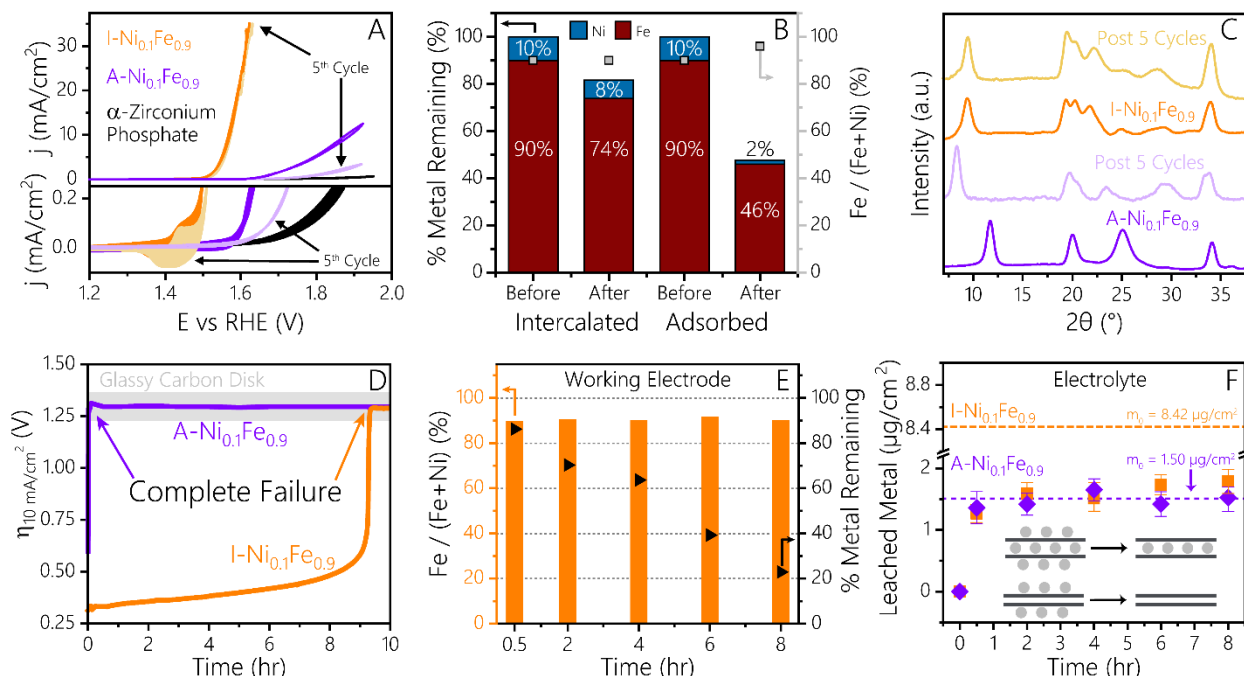
Figure 3 – Electrochemical stability studies for adsorbed and intercalated $Ni_{0.1}Fe_{0.9}$ catalysts in a 0.1 M KOH electrolyte. (A) Cyclic voltammetry of adsorbed and intercalated $Ni_{0.1}Fe_{0.9}$ catalysts showing the first and fifth cycle. The 1st cycle is shown in orange (I-$Ni_{0.1}Fe_{0.9}$) and purple (A-$Ni_{0.1}Fe_{0.9}$) while the fifth cycle is shown in a lighter color in comparison to the original 1st cycle. Inset plot below shows the redox features exhibited by the I-$Ni_{0.1}Fe_{0.9}$ catalyst in the same potential window as the above panel with the same legend. Corresponding plots of the amount of (B) metal remaining on the working electrode (left axis) and final composition (right axis – gray squares) after five cycles through ICP-MS analysis. (C) XRD of the adsorbed and intercalated $Ni_{0.1}Fe_{0.9}$ catalysts after five cycles. (D) Chronopoteniometry of adsorbed and intercalated $Ni_{0.1}Fe_{0.9}$ catalysts. The light-gray shaded region represents the overpotential range exhibited by a pristine glassy carbon disk to achieve η_{10}. (E) Corresponding plots of Fe / (Fe + Ni) composition and remaining metal on the working electrode for an intercalated $Ni_{0.1}Fe_{0.9}$ catalyst. (F) ICP-MS analysis of the electrolyte quantifying the amount of leached metal (Ni and Fe species) for adsorbed and intercalated $Ni_{0.1}Fe_{0.9}$ catalysts during chronopotentiometry. Schematic within the panel represents a possible interpertration of the leached metal data where adsorbed species dissolve from the outer surface of both A- and I-$Ni_{0.1}Fe_{0.9}$ catalysts.

By cyclic voltammetry (5 cycles) we see that the I-$Ni_{0.1}Fe_{0.9}$ has a significant Ni redox (+2→ +3) feature centered around 1.43 V vs RHE (**Figure 3A**). This feature is common in layered Ni/Fe materials and is observed for all of the mixed-metal intercalated systems (**Figure S4A and C**).[9] Furthermore, after 5 CVs, the activity, nickel redox features, Ni/Fe ratio, Zr/P ratio, and interlayer spacing remain relatively constant. (**Figure 3A-C and Figure S5)**. Specifically, the η_{10} at the fifth cycle is 8 mV higher when compared to the first cycle. By digesting the working electrode in aqua-regia after the moderate electrochemical cycling we were able to monitor the Ni and Fe species remaining after catalysis via ICP-MS. We see ~20% total losses in Fe and Ni species for the I-$Ni_{0.1}Fe_{0.9}$ catalyst and it retains its as prepared composition of 90% Fe. This retention of high Fe content is particularly interesting because typically high Fe-containing catalysts have been

274 seen to disproportionally dissolve Fe due to FeO_x phase segregation.[54] There have been increasing

275 concerns that some of the current we have attributed to OER is actually from metal dissolution or

276 carbon corrosion.[55–57] For this reason, we examined the possibility as to whether part or all of

277 current observed during the first cycle could originate from Fe or carbon corrosion. Based on our

278 calculations (**see SI for details**), total Fe or carbon corrosion would correspond with ~ 0.74% and

279 ~ 104% of the total charge passed during the first cycle, respectively. For Fe, because total

280 dissolution would impact < 1 % of the current it is unlikely that Fe corrosion contributes

281 substantially to the observed current. Furthermore, the lack of impact on the current from C

282 corrosion is showcased by the intercalated current stability over 5 cycles (a level of stability that

283 would not have been possible if 20 % of the C corroded each cycle). Additionally, as shown in

284 **Figure S6**, if all the C black were to corrode there would be no activity without the conductive

285 backbone. The retention of the majority of the Ni/Fe species, an unperturbed interlayer spacing,

286 and OER stability support the hypothesis that the Ni/Fe species remain within the interlayer during

287 catalysis.

288 In contrast to I-$Ni_{0.1}Fe_{0.9}$, the cyclic voltammetry for A-$Ni_{0.1}Fe_{0.9}$ shows that the Ni-redox

289 wave is not present in any cycle for the adsorbed catalysts and for all other adsorbed systems

290 (**Figure S4B,D**). This could suggest that the Ni species adsorbed on the surface of the zirconium

291 phosphate sheets are not electrochemically accessible/active or that they do not remain on the

292 surface during electrochemical evaluation. Furthermore, after 5 cycles (**Figure 3A**), we see that

293 the A-$Ni_{0.1}Fe_{0.9}$ lost 87% of its maximum activity (25 to 1.4 mA/cm^2 at 1.8 V vs RHE) and

294 approaches the activity of pristine zirconium phosphate. However, as seen by ICP-MS, the A-

295 $Ni_{0.1}Fe_{0.9}$ only loses ~50 % of its total metal content (**Figure 3B**). There is disproportional Ni-

296 dissolution and the final composition has only 4 % Ni relative to Fe. Notably, the amount (1.4 ±

297 0.1 $\mu g/cm^2$) of Ni/Fe that was lost when the I-$Ni_{0.1}Fe_{0.9}$ was cycled nominally matches the total

298 amount (1.5 ug/cm^2) of species contained by A-$Ni_{0.1}Fe_{0.9}$. We hypothesize that only adsorbed

299 Ni/Fe species dissolve for both systems, likely because intercalated Ni/Fe species are strongly

300 coordinated within the zirconium phosphate sheets, as discussed later in the computational section.

301 It also suggests that the Ni redox as seen by the intercalated catalyst is not from Ni/Fe species

302 adsorbed to the surface. XRD of the cycled catalyst shows an expansion in the interlayer spacing

303 from 7.6 to 10.6 Å. This level of expansion is consistent with a final structure that is similar that

304 of a fully expanded θ-zirconium phosphate, and could be due to either hydration and/or potassium
305 intercalation during the catalysis (**Figure S7-8**). It is interesting to note that the final A-$Ni_{0.1}Fe_{0.9}$
306 layer spacing is ~1.4 Å larger than that of the I-$Ni_{0.1}Fe_{0.9}$, which remains at a constant interlayer
307 spacing of ~9.2-9.3 Å, suggesting that intercalated Ni/Fe species alter the dynamics of dissolution,
308 hydration, and/or potassium intercalation during catalysis. Despite the poor activity and the lack
309 in redox wave, the slight OER activity above that of zirconium phosphate and the partial retention
310 of Ni/Fe species indicates that that within our moderate cycling of the A-$Ni_{0.1}Fe_{0.9}$ we are indeed
311 probing adsorbed species electrochemically.

312   To assess the longer-term stability of the I-$Ni_{0.1}Fe_{0.9}$ and A-$Ni_{0.1}Fe_{0.9}$ systems during
313 catalysis we monitored the Ni and Fe content for ~ 8 h at 10 mA/cm^2. The chronopotentiometry
314 (CP) (**Figure 3D**) shows that the A-$Ni_{0.1}Fe_{0.9}$ catalyst rapidly degraded in less than 72 seconds,
315 while the I-$Ni_{0.1}Fe_{0.9}$ was dramatically more stable (by an order of magnitude) with only ~19
316 mV/hr decay in performance during nine hours of continuous operation. After nine hours we see
317 rapid and complete catalytic failure. This type of catalytic failure has been previously associated
318 with substrate failure.[56,57] ICP-MS analysis (**Figure 3E**) of the working electrode shows that the
319 Fe/Ni ratio remains constant at 90% for the duration of the experiment. However, a loss in the total
320 Ni/Fe content is observed throughout the duration of the experiment. Specifically, at 30 mins, 84%
321 of the Ni and Fe metal content remain on the electrode. As time increases, the amount of metal
322 remaining drops to 65, 61, 39, and 22% for 2, 4, 6, and 8 hours respectively. Analysis of the
323 working electrode (**Figure S9**) indicates that the loss in active mass might be attributed to
324 concomitant carbon corrosion/delamination as well Ni/Fe dissolution. To decouple delamination
325 and dissolution, in conjunction with the ICP-MS analysis of the working electrode, ICP-MS
326 analysis was also performed during the CP via aliquots taken from the electrolyte. Analysis of the
327 Fe and Ni dissolved in the electrolyte (**Figure 3G**) reveals that nearly all the dissolution occurs
328 within 30 min of testing, illustrating that the majority of loss of activity is possibly due to catalysts
329 dissolution. Interestingly, a similar mass dissolution of ~1.50 µg/cm^2 into the electrolyte is shown
330 for the intercalated (P-3) system within 30 minutes for the duration of the experiment. In agreement
331 to previous grafting experiments, the electrolyte analysis indicates that the activity of the I-
332 $Ni_{0.1}Fe_{0.9}$ catalyst occurs mostly within the bulk of the interlayers since an equal mass loss to that
333 of surface bound adsorbed species is found to dissolve during electrochemical testing. Since the

14

334   carbon is shown to delaminate during testing, it is hypothesized that active material goes into

335   solution and does not dissolve; therefore, we will only see the mass of Fe and Ni species from this

336   delaminated catalyst layer if it chemically dissolves since solids are filtered out during aliquot

337   testing for ICP-MS analysis. This analysis, accentuated by activity, structural, and ICP-MS data,

338   supports the hypothesis that for both systems, adsorbed species dissolve from the outer sheets of

339   zirconium phosphate. This understanding along with the stability of the interlayer allows us to

340   further probe the activity of the confined Ni/Fe catalysts.

341   ***Active Ni/Fe Species within the Zirconium Phosphate Layers.***

342   There have been several examples in which a specific local environment plays a deciding

343   role in the properties of an active site.[19,21] Our confined layered Ni/Fe catalysts (P-3) have a

344   unique, well-defined environment and the Ni/Fe species remain within the layers during catalysis.

345   To determine if the origins of the enhanced activity are within the interlayer, we conducted a series

346   of electrochemical experiments (**Figure 4**) focused on probing the kinetics (Tafel plots) and

347   location of active species (surface grafting). In depth analysis of the rate of OER turn-on as a

348   function of overpotential, e.g. Tafel slope, have been used to compare the reaction kinetics of

349   different catalytic materials. A Tafel slope values of the polarization curves (**Figure 4C**) shows

350   that I-$Ni_{0.1}Fe_{0.9}$ not only reduces the onset potential, but also has a substantial lower Tafel slope of

351   41 mV/dec compared to the 220 mV/dec of A-$Ni_{0.1}Fe_{0.9}$. The Tafel slope of 41mV/dec is

352   particularly interesting since it is similar to that of a layered double hydroxide (LDH) system

353   suggesting the same rate limiting step (RLS). [9] However, these values are commonly obtained for

354   a Ni-rich Ni/Fe LDH system, and not for the Fe-rich system reported here. A similar Tafel slope

355   could also indicate that a similar catalytic motif to that of a LDH has been made within the confined

356   space of zirconium phosphate sheets albeit at a high Fe content, as discussed later in the

357   computational section. Furthermore, a reduced Tafel slope (**Figure S10**) is found to only common

358   to the mixed metal P-3 systems as opposed to P0 ones.

359   In order to determine if the confined Ni/Fe species are catalytically active in the interlayer

360   during catalysis, the performance and electrochemical profile of A- and I- $Ni_{0.1}Fe_{0.9}$ catalysts were

361   compared after displacing surface-adsorbed Ni/Fe species (**Figure 4D-F**). In this case, with surface

362   catalytic sites displaced, any activity would be due to intercalated species. To remove the surface
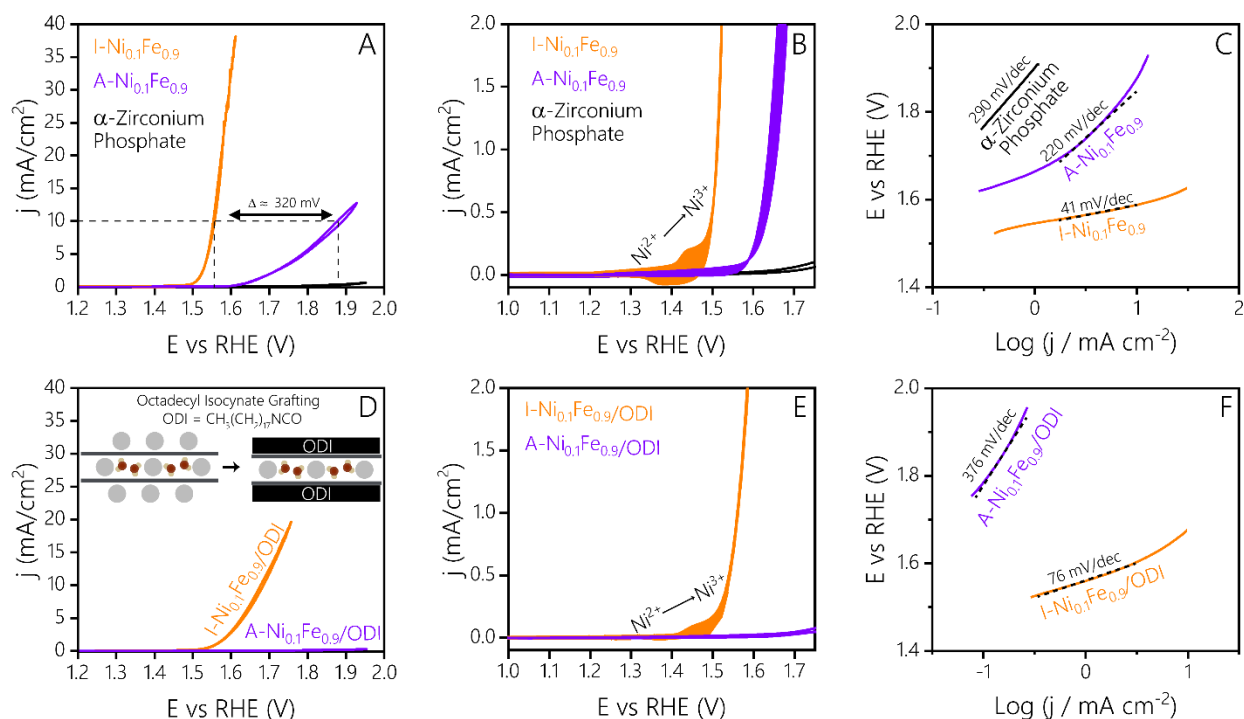
Figure 4 – Cylcic voltammetry studies for (A) adsorbed (purple) and intercalated (orange) $Ni_{0.1}Fe_{0.9}$ catalysts and (B) zoomed in view of panel A to showcase the Ni redox feature. (C) Tafel plots for adsorbed and intercalated $Ni_{0.1}Fe_{0.9}$ catalysts. (D) Cyclic voltametry studies for ODI modified adsorbed and intercalated $Ni_{0.1}Fe_{0.9}$ catalysts and (E) zoomed in view of panel D to showcase the Ni redox feature. (F) Tafel plots for ODI modified adsorbed and intercalated $Ni_{0.1}Fe_{0.9}$ catalysts.

363   sites we synthesized A- and I- $Ni_{0.1}Fe_{0.9}$ catalysts as described above, subsequently grafted with

364   octadecyl isocyanate (ODI) following literature protocol,[58] and assessed for the OER. Successful

365   grafting, resulting in the displacement of surface bound metal species, was confirmed through the

366   electrochemical inactivity of the ODI-modified A-$Ni_{0.1}Fe_{0.9}$ catalyst (**Figure 4D**). Conversely, for

367   the intercalated ODI-modified catalyst, electrochemical activity is modestly reduced and the Ni

368   redox remained apparent (**Figure 4E**). These findings suggest that 1) the species at the interlayer

369   are active for the OER and 2) Ni-based species remain electrochemically accessible within the

370   interlayer. The catalytic performance of the grafted I-$Ni_{0.1}Fe_{0.9}$ is lower than that of the non-grafted

371   system and the Tafel slope (**Figure 3F**) of I-$Ni_{0.1}Fe_{0.9}$ /ODI is ~ 2x higher than its' non-grafted

372   counterpart. We postulate that this observed difference in activity could stem from hindered water

373   transport to the interlayer due to the hydrophobic ODI molecules grafted to the surface of

374   zirconium phosphate. To our knowledge, this is the first time where it has been clearly shown that

375   the interlayer is active for the OER for confined layered catalysts. To investigate the interlayer

376　enhancement, assessments on the systems structure (DFT calculations), composition (Fe
377　oxidation), and environment (water content) are presented below.

378　*Computational Analysis of the Intercalated Zirconium Phosphate Structure*

379　　　　In order to investigate the structural identity and activity of the confined motif within the
380　interlayer of zirconium phosphate, DFT and a thermodynamic approach to the OER were
381　employed. As expected from the ion-exchange chemistry of zirconium phosphate, our calculations
382　find that removal of the exchangeable proton at the OH of the phosphate group is necessary for
383　any bond formation to occur with the layers. Based on the available crystal structures within the
384　literature and the ICSD database, we have identified wycheproofite, $NaAlZr(PO_4)_2(OH)_2 \cdot H_2O$
385　(ICSD:55430) as a host platform to simulate P-3 catalysts (**Figure 5**).[50,59,60] This host platform
386　allowed for a stable octahedral configuration of intercalated 3+ cations. Other coordinations, tested
387　only for α-phase are shown in **Figure S11**. Specifically, when octahedral Al^{3+} is substituted by
388　Fe^{3+}/Ni^{3+}, the fully optimized structure has very similar XRD features as the $I-Ni_{0.1}Fe_{0.9}$ catalyst
389　(**Figure 5A**), which remains unchanged for other simulated Fe/(Fe+Ni) ratios (**Figure S12)**. We
390　assume that Fe^{3+} can occupy Al^{3+} sites as its often observed for earth crust crystals and for NiOOH
391　systems.[61,62] Molecular dynamics showcase Fe ion adsorption on inner layers of Ni/FeOOH, which
392　result in a similar octahedral intercalation motif.[63] Additionally, as shown in **Figure S7**,
393　replacement of Na^+ with K^+ is possible due to intercalation of solvated K^+ species from KOH
394　electrolyte. The resulting wycheproofite-type structure (*$K(Ni_xFe_{1-x})O_2$ $Zr(HPO_4)_2 \cdot H_2O$*, **Figure
395　5B**) with an interlayer distance of 8.9 Å features octahedral zig-zag chains of intercalated Fe^{3+} and
396　Ni^{3+} cations connected to zirconium phosphate layers via two phosphate groups per cation, similar
397　to that observed in bulk olivine-type $Li(Fe/Ni)PO_4$.[64] While there is high correlation between the
398　observed XRD features and simulated structure, we note that this structure is one possible
399　representation of Ni and Fe species within the interlayer of our catalyst. Nevertheless, the
400　simulated structure represents a good model for octahedral bonding of cations within the interlayer
401　where bonding occurs via phosphate groups.
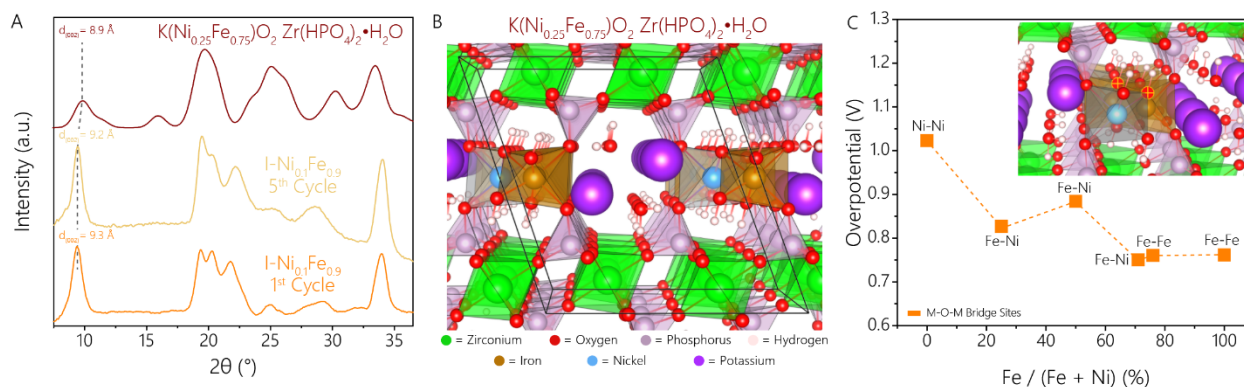
Figure 5 – **(A)** Comparission of the XRD patterns fo the simulated $K(Ni_{0.25}Fe_{0.75})O_2\ Zr(HPO_4)_2 \cdot H_2O$ (dark red) with the meassured intercalated I-$Ni_{0.1}Fe_{0.9}$ catalyst after 1 and 5 cycles (orange and yellow, respectively). For direct comparison with experiemnt, a gaussian broadening was of applied to calculated XRD. The corresponding XRD paterns for other Fe/(Fe+Ni) ratios are shown in **Figure S12 (B)** Detailed view of simulated wycheproofite structure $K(Ni_{0.25}Fe_{0.75})O_2\ Zr(HPO_4)_2 \cdot H_2O$ highlighting the chains (Fe/Ni)O_6 octahedra bonding (orange/blue) to tetragonal PO_4 groups (purple). **(C)** Calculated trends in the OER activities based on the structure (B) as fucntion of the Fe/(Fe+Ni) ratio. The metal-O-metal (M-O-M) bridge activity of the bulk-sites trend is shown as orange squares, with labels indicating the type of the metals in the bridge. Inset on the top-right correponds to a zoom in of the panel shown in (B) with highlighted (yellow circle outline) oxygen active sites.

402   The theoretical activities of the bulk sites within the simulated structure were assessed from

403   calculated adsorption thermodynamics of OH*, O* and OOH*.[65–67] In our analysis, Zr^{+4} and PO_4^{-3}

404   sites were calculated as inactive towards OER, acting as strong Lewis acid pairs to oxygen's

405   Lewis base. In **Figure 5C**, we highlight the calculated trends in OER activity as function of the

406   Fe-Ni ratio. Specifically, we assess the activity of M-O-M bridge sites which feature double

407   coordinated oxygen (O_{2c}) in the octahedral chains of the simulated bulk structure. Our results show

408   that presence of Fe next to Ni (Fe-O-Ni bridge sites) is beneficial for the OER activity, reducing

409   the OH* to O* potential limiting step (PLS) for Fe-Ni mixtures. The origin of this effect is mostly

410   electronic, where high-spin Fe^{+3} binds O_{2c} much stronger than low-spin Ni^{+3}. Similar results are

411   found with top-site binding in NiFeOOH studies, which is combined with minor structural effect,

412   where the Fe^{+3} cation with larger ionic radius expand the lattice relative Ni^{+3} cation.[65,68,69] The

413   local minimum in overpotential is achieved for Fe-O-Ni at 75% Fe content, which agrees well

414   with the results observed for P-3 systems (**Figure 2C,D**). The calculations for Fe-O-Fe bridge sites

415   with 100% Fe also indicate high activity, though experiments for this system show low

416   conductivity (**Figure 2B**) and instability (**Figure S9**) compared to Ni-containing rich P-3 systems.

417   Trends in our octahedral intercalation model are consistent with observed experimental

418   trends. To further understand the variability within the system theoretically we probed the role that

419   modifying other factors such as K^+ removal, surface activities at phosphate, and metal terminated

420   (001) surfaces play in lowering the overpotentials from bulk intercalated values (~0.8 V). While

421   these structures are not accessible thermodynamically with our current synthesis, theoretically, we

422   show that replacing the PO_x groups with Fe could be an interesting method for improving the

423   activity (**Figure S13 A,B**). Furthermore, there are additional influences in the intercalated system

424   that arise from a confined catalyst environment, including the effect of water and the electronic

425   structure of the Ni/Fe network that can have a role on the observed activity trends. To that end, we

426   extend our experimental understanding of the possible effects that may influence activity within

427   the confined space by assessing the interlayer through x-ray absorption spectroscopy and

428   thermogravimetric studies.

429   ***Interlayer Environment is Important for Enhancement***.

430   The assessment of composition, loading, conductivity, structure, activity, and leaching for

431   the I-$Ni_{0.1}Fe_{0.9}$ catalyst has shown that intercalated species are active and responsible for the

432   majority of the observed OER activity. It is clear that composition and interlayer environment

433   provided by P-3 systems are important in both stabilizing and activating Ni/Fe species within

434   zirconium phosphate. Therefore, to expand on experimental and DFT studies where a high Fe

435   content achieves high activity, we further assessed how confinement of Ni/Fe species could affect

436   the interlayer environment (interlayer water) and/or Ni/Fe properties (oxidation state).

437   Specifically, we find experimental evidence that an elevated Fe oxidation state and an optimum of

438   interlayer water content correlate with improved activity (overpotential and mass activity,

439   respectively) for P-3 systems.

440   A large body of work has found that Fe exists at an elevated oxidation state and ex-situ and

441   operando measurements have found +3, +4, and +5 oxidation states for Fe-based catalysts. [10,65,70–

442   72] Furthermore, Fe has also been linked to the enhanced electrocatalytic activity observed in these

443   systems.[65,73,74] Thus, we measured Fe-L edges through x-ray absorption spectroscopy (XAS) for

444   as-prepared P-3 catalyst powders and assessed their Fe^{3+} content with activity trends. XAS

445   measurements (**Figure S14A**) show both Fe^{2+} and Fe^{3+} within the spectrum and give insight

446   regarding the electronic interactions between Ni and Fe.

447   The integral Fe $L_{2,3}$-edge white-line intensity ratios were used to quantify the total number

448   of ferric (Fe^{3+}) iron content for as-prepared intercalated P-3 systems.[75] For these catalysts systems,

449   η_{10} (**Figure S15**) is shown to improve with an increase in Fe^{3+} content while a slight optimum is

450   obtained for mass activity (**Figure S14B**). Specifically, the two intercalated catalysts I-$Ni_{0.1}Fe_{0.9}$

451   and I-$Ni_{0.5}Fe_{0.5}$ with the lowest η_{10} (340 and 370 mV, respectively) exhibit the higher Fe^{3+} wt%

452   suggesting that Fe^{3+} is important for activity (**Figure S15C**) and higher Fe^{3+} content is observed

453   with increasing Fe content in P-3 systems (**Figure S15D**). Furthermore, when comparing an

454   adsorbed to an intercalated system (**Figure S16**), we find that for I-$Ni_{0.1}Fe_{0.9}$ catalyst, Fe exists at

455   higher ferric concentrations (80%) versus an A-$Ni_{0.1}Fe_{0.9}$ (69%) or an I-Fe (63%) system.

456   Additionally, when comparing Ni-L edges (**Figure S17**), an increase in Fe content leads to an

457   increase in Fe^{3+} content and reduced Ni species indicating a partial electron transfer Fe to Ni and

458   that the interlayer environment plays a role in modulating the oxidation state of the intercalated

459   species.

460   With regards to the role that the environment plays in enhancing catalysis, molecular

461   dynamic simulations have shown that confined spaces can create frustrated solvation structures

462   (partial solvation shell) such as frustrated water, that have a profound effect on electron transfer

463   through enhanced energy gap fluctuations beyond those expected from Marcus theory.[17,27,76]

464   Zirconium phosphate is a model system to use as a platform to confine Ni/Fe species within the

465   interlayer since it is well known that negatively charged zirconium phosphate sheets interact

466   strongly with water, competing with its hydrogen-bond network.[53] Due to the abundant number of

467   interlayer cations and the confined space within the interlayer of zirconium phosphate which does

468   not allow for a full solvation shell, the solvation shell of water surrounding Ni and Fe species

469   would potentially result in a partial solvation shell. This partial solvation shell is known as

470   frustrated water and has shown enhancements in electron transfer within catalyst materials.[17,76]

471   While the structure/order of water in layered materials can be assessed through neutron

472   diffraction/scattering studies,[77,78] distinct types of water (free vs. bounded water) can also be

473   identified through thermogravimetric analysis (TGA) of the as-prepared zirconium phosphate

474   catalyst powders.[53]
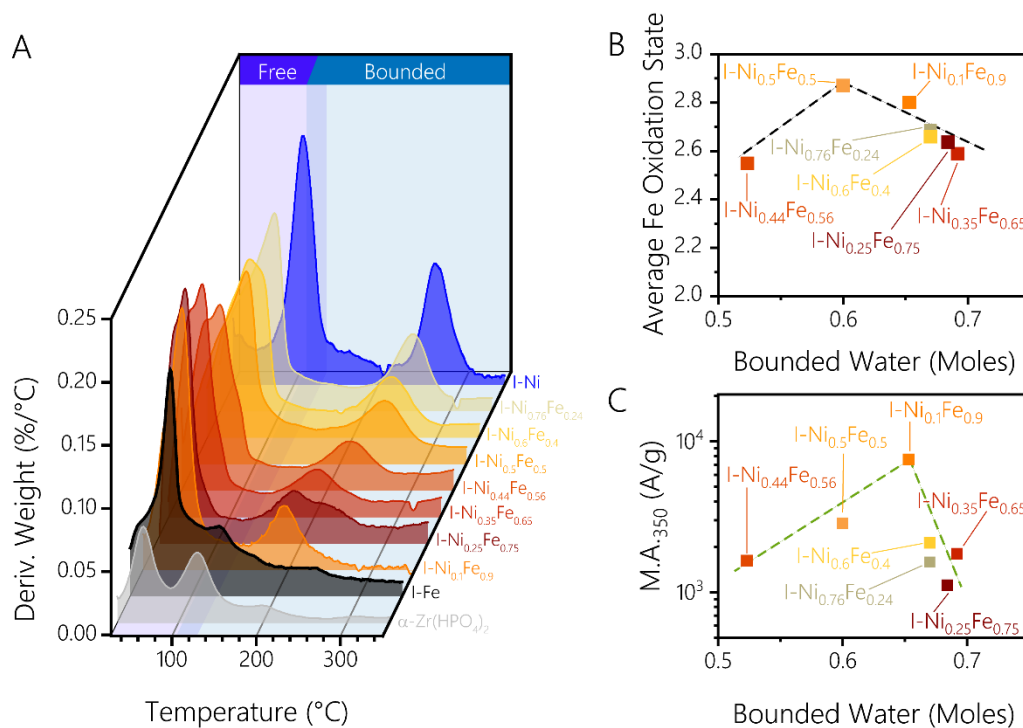
Figure 6 – (A) TGA measurements under N_2 flow showcasing the derivative of the weight loss with respect to temperature for intercalated catalysts as a function of Fe % relative to Ni. **(B)** respective average Fe oxidation state and **(C)** M.A. at 350 mV overpotential as a function of moles of bounded water.

475   In TGA measurements, the removal of weakly coordinated water (free water) is associated
476   with the first dehydration event and is usually observed below 90-120 °C. The second dehydration
477   event that occurs at higher temperatures and corresponds to strongly coordinated water (bounded
478   water) and herein is considered to be frustrated. **Figure 6A** shows two distinct weight loss regions
479   for all intercalated systems and are shown as separate panels in **Figure S18A-H** for clarity. The
480   total water content of intercalated samples (**Figure S18I**) is found to be between 2.3-2.7 moles of
481   water per mole of zirconium and is similar to previous reports of intercalated metal systems.[79] In
482   terms of activity, an optimum for performance is found with respect to overpotential and mass
483   activity (**Figure 6C**) for bounded water at 0.65 moles of water per mole of zirconium. As the total
484   bounded water increases above 0.65 moles of water per mole of zirconium, it is possible that a
485   more complete solvation shell forms which might mitigate the effect of improved electron
486   transfer.[17,18] XAS and TGA data shows that a specific oxidation state correlates with a specific
487   amount of bounded water (or vice versa) and high activity. We hypothesize that the composition
488   (including oxidation state) of the intercalated structures and the amount of bounded water play a
489   role in controlling the activity of the catalysts (**Figure 6B and Figure S19**) due to an optimum

490 observed for the average iron oxidation state and bounded water. However, we note that these
491 systems are inhomogeneous within the interlayers due to the absence of a trend when comparing
492 composition to iron and water content (**Figure S20**); therefore, decoupling water content and
493 oxidation state is necessary to further understand how the bulk properties of P-3 systems are
494 affected by the co-intercalation of Ni and Fe cations. Additionally, future studies such as
495 dehydration studies for the removal of water and its dependence on Fe^{3+} content and activity, which
496 are out of the scope of this work, would be necessary to elucidate these dynamics during operando
497 conditions. This new understanding of the role of environment (frustrated water) and cation
498 properties (oxidation state) could be used in the future to modify future reactions in confined
499 spaces. Specifically, highly hydrated cations that strongly retain water and that are catalytically
500 active for the OER (Ni^{2+}, Co^{2+}, Fe^{3+}) along with cations that strongly retain water but are not
501 catalytically active (Al^{3+}, Cr^{3+}, Ga^{3+}, Be^{2+}, Mg^{2+}) are interesting species to co-intercalate to modify
502 the amount of interlayer water and assess their role on activity. This work provides a platform for
503 studies focused on elucidating the origins of improved intrinsic activity for future confined layered
504 catalyst systems.

505 **Conclusions**

506 In this work we demonstrate an active catalyst motif based on transition metal cations
507 confined within environments of molecular length scales. This motif contains Ni and Fe cations
508 that are bonded to phosphate groups within the water-containing layered structure of zirconium
509 phosphate, producing highly active Fe-rich OER catalysts. We show that modifying the
510 homogeneity of interlayer environment can improve the activity and stability for the OER in a
511 confined space. Improved intrinsic activity is achieved only for mixed metal systems that are fully
512 intercalated. Grafting studies indicate that the activity originates from the species within the
513 interlayer and not those that are surface bound. Computationally, we find that a wycheproofite
514 type structure represents a suitable platform for the octahedral intercalation of cations were
515 bonding occurs via phosphate groups. In this system, by increasing Fe content in M-O-M sites
516 there is a reduction of the OH* to O* potential limiting step (PLS) for Fe-Ni mixtures, due to high-
517 spin Fe^{+3} binding O_{2c} much stronger than low-spin Ni^{+3}. Overall, the enhancement in activity and
518 stability is postulated to originate from the confined environment provided by zirconium phosphate

519 which allows for the synergism with Ni/Fe species and confined water molecules. Future

520 refinement of the catalyst structure along with additional computational analysis and

521 considerations will be necessary to fully understand the role of the interlayer environment. We

522 anticipate that property tuning within confined systems via interlayer engineering is a promising

523 strategy towards further enhancing performance for water oxidation, as well as other reactions of

524 interest.

525 **Experimental Procedures:**

526 **Materials**

527 All chemicals were obtained from commercial sources as analytical or reagent grade and used as

528 received. Iron sulfate heptahydrate ($FeSO_4 \cdot 7H_2O$, 99.5%), nickel nitrate hexahydrate

529 ($Ni(NO_3)_2 \cdot 6H_2O$, 98.5%), Nafion 117 (5% solution), zirconyl chloride octahydrate ($ZrOCl_2 \cdot 8H_2O$,

530 98%), octadecyl isocyanate ($CH_3(CH_2)_{17}NCO$, $\geq$ 90%), and o-xylene ($C_6H_4(CH_3)_2$, analytical

531 standard) were obtained from Sigma-Aldrich (St. Louis, MO). Phosphoric acid (H_3PO_4, 85%) was

532 obtained from Fisher Scientific (Hampton, NH). Glassy carbon rods (SIGRADUR G, HTW

533 Hochtemperatur-Werkstoffe GmbH, 5 mm diameter) were processed by the Stanford University

534 crystal shop to the specifications of a 4 mm height and an area of 0.196 cm^2 where the top side

535 was polished to a surface root-mean-square (rms) roughness of <50 nm. Carbon black was

536 purchased from Fuel Cell Store (College Station, TX, Vulcan XC-72).

537 **Synthesis**

538 **θ-Zirconium phosphate:** The synthesis of θ-zirconium phosphate was adapted from a

539 literature method.[49] In brief, 100 mL of a 0.05 M solution of $ZrOCl_2 \cdot 8H_2O$ in deionized water was

540 added dropwise (2 ml min^{-1}) to 100 mL of a 0.06 M H_3PO_4 solution that was preheated to 94 °C.

541 This mixture was magnetically stirred for 48 hours at 94 °C. The product was then centrifuged

542 (10,000 RPM for 30 mins) and washed several times (3 times minimum) with deionized water

543 (18.2 MΩ·cm, Merck Millipore, Billerica, MA, USA) and resuspended in a deionized water

544 solution for storage.

545 **α-Zirconium phosphate:** θ-zirconium phosphate was converted to α-zirconium phosphate

546 by obtaining a θ-zirconium phosphate gel after centrifuging (10,000 RPM for 30 mins) and

547 subsequently drying it in a vacuum desiccator for > 48 hours. The dried solid was then grounded

548   into a fine powder with a mortar and pestle. Confirmation of successful removal of excess water

549   was confirmed by XRD.

550   **P-0, P-1, P-2, and P-3 Catalyst Synthesis:** For P0 catalysts, 30 mg of α-zirconium

551   phosphate in 1 mL of deionized water was used as the precursor material and mixed with 1 mL of

552   a metal salt precursor solution. The metal solution consisted of metal salt precursor

553   ($Fe(NO_3)_2 \cdot 6H_2O$ and/or $Ni(NO_3)_2 \cdot 6H_2O$) at varying metal:α-Zirconium phosphate molar ratios

554   (M:zirconium phosphate). This solution was added to the 1.0 mL suspension of α-zirconium

555   phosphate and left stirring for 48 h. The molar ratios were varied from 10:1 to 1:10 M:zirconium

556   phosphate to produce the various compositions of Ni/Fe modified P0 zirconium phosphate

557   catalysts. For P-1, P-2, and P-3 catalysts, θ-zirconium phosphate was used instead of α-zirconium

558   phosphate.

559   **ODI Modified Zirconium Phosphate:** ODI modification of adsorbed and intercalated

560   catalysts followed an adapted procedure from the literature.[58] In short, adsorbed and intercalated

561   zirconium phosphate catalysts were modified by ODI in a three-necked flask. 10 mg of the

562   zirconium phosphate catalyst was dispersed into 25 mL of o-xylene in a three-necked flask and

563   sonically dispersed for 2 hours. ODI was added to the dispersed system at a molar ratio of 10:1 for

564   catalyst to ODI. The mixture was then reacted for 12 hours under nitrogen gas. The mixture was

565   then centrifuged at 10,000 RPM for 30 mins and the product was washed with ethanol several

566   (>3x) times to remove impurities. The ODI modified catalyst was then vacuum dried for 24 hours

567   where the dried solid was then grounded into a fine powder with a mortar and pestle.

568   **Ink Preparation**

569   Modification of the GCD with the catalyst was performed by spin drying a 10 μL drop of

570   the catalyst ink which consisted of the catalyst powder, isopropanol, carbon black, and cation-

571   exchanged Nafion 117 at 600 RPM on the RDE apparatus. The cation-exchanged Nafion 117 was

572   prepared by dissolving 2 mL of Nafion 117 into 1 mL 0.1M KOH. As Nafion is a strong acid,

573   through this process, H^+ is replaced with K^+ to keep the ink condition similar to the electrolyte.

574   Each catalyst ink was prepared by dispersing 5 mg of the catalyst and 1.25 mg of carbon black in

575   2.55 mL of isopropanol and 10.02 μL of cation-exchanged Nafion 117. The ink was sonicated for

576   >30 minutes or until it was well dispersed. The loading of the working electrode was 100 μg cm^{-2}

577   of catalyst material and 25 μg cm^{-2} of carbon black for a total catalyst loading of 125 μg cm^{-2}. To

578   obtain the amount of Ni/Fe metal content within each catalyst, the wt% was multiplied by 100 μg

579   cm^{-2}.

580   **Electrochemical Measurements**

581   Electrochemical measurements were performed on a VMP-3 potentiostat/galvanostat

582   (BioLogic Science Instruments). Four-point probe measurements were conducted on compressed

583   catalyst powders (15 mg in a 6 mm diameter die at 2000 lbs of applied load) using an in-line four-

584   point probe with 1 mm tip spacing (Lucas Labs, Pro4-4000). Oxygen evolution studies were

585   carried out on a three-electrode electrochemical cell using a rotating disk electrode (RDE)

586   assembly (Pine Research Instrumentation). OER measurements were performed between 0.2 and

587   1.0 V versus the silver/silver chloride couple (Ag/AgCl) at 10 mV s^{-1} in O_2- saturated 0.1 M KOH

588   electrolyte with an Ag/AgCl reference electrode (Fisherbrand accumet Glass Body Ag/AgCl

589   Reference Electrode – Mercury-Free, Thermo Fischer). The counter electrode was calibrated

590   between each batch of new electrolyte. The counter electrode was a graphite rod and the working

591   electrode was a clean, mirror finish-polished, 5 mm diameter glassy carbon disk (GCD) modified

592   with a zirconium phosphate catalyst. During electrochemical measurements, the working electrode

593   was rotated at 1600 rpm. The rotation speed was fast enough to help in product removal from the

594   surface and limit the bubble formation from oxygen evolution. The solution resistance of the cell

595   was measured at 100 kHz with 20 mV amplitude about the open-circuit potential (OCP), and iR-

596   drop compensation occurred after electrochemical testing. The typical solution resistance was 44

597   – 55 Ω. All potentials were converted and reported herein versus the reversible hydrogen electrode

598   (RHE).

599   **Physical and Chemical Characterization (XRD, ICP-MS, TEM, XAS, and TGA)**

600   X-ray diffraction data were obtained using a D8 VENTURE single-crystal diffractometer

601   (Bruker, λ = 1.5418 Å). The concentration of Fe and Ni of the electrodes and electrolyte was

602   obtained through inductively coupled plasma mass spectrometry (Thermo Scientific, XSERIES 2

603   ICP-MS). All working electrode samples were digested overnight in an aqua regia matrix before

604   analysis. For electrolyte analysis, aliquots (4 mL) were taken after 0.5, 2, 4, 6, and 8 hr of CA

605   testing fresh electrolyte (0.1 M KOH - 4 mL) was replenished such that the total volume of

606   electrolyte was unchanged. All calibration standards were TraceCERT certified and obtained from

607   Sigma-Aldrich. All XPS spectra were calibrated to the C 1s peak at a binding energy of 284.8 eV.

608   CasaXPS software was used to perform peak fitting with Shirley backgrounds. X-ray absorption

spectroscopy was performed at the Stanford Synchrotron Radiation Laboratory (SSRL) in total electron yield mode at beamline 8-2 for the Fe and Ni L-edge. For all experiments, powdered samples were dispersed on carbon tape. For Fe and Ni L-edge spectroscopy, edge-energies were aligned to Ni foil standard sample. All XAS spectra (n=7) were averaged and processed with the Demeter package in Athena. A universal Fe analysis, as described by the literature, was performed on the normalized white line intensities Fe $L_{2,3}$-edges to quantify the amount of ferric iron within zirconium phosphate catalysts.[75] Thermogravimetric experiments (TGA Q500 TA Instruments, New Castle, Delaware, United States) were performed at a ramp rate of 5 °C min^{-1} up to 400 °C under a flow of 100 mL/min of nitrogen gas.

Computational Methods

The density functional calculations were performed within the Vienna ab initio simulation package[80,81] (VASP) using the projector augmented wave (PAW) potentials[82]. We employed the PBE[83] functional together with the Hubbard-U correction method[84] applied for the d-electrons of Ni (U-J=U_{eff} = 6.0 eV) and Fe (U_{eff} = 3.5 eV) atoms[69,85]. The bulk optimization calculations were performed at the energy cutoff of 600 eV on the $4 \times 4 \times 4$ k-point mesh per $2 \times 1 \times 1$ unit cell of the wycheproofite structure. For surfaces, we have employed 2×1 symmetric (001) slabs. Here we used 500 eV energy cutoff and the $4 \times 4 \times$ k-points. Full relaxation below a minimum threshold force of 0.02 eV/Å^2 was performed in all cases. To obtain the theoretical overpotential for each bulk and surface site, the standard OER mechanism and which has been applied to many types of oxides[65–67,86] ($* \rightarrow$ OH*, OH* $\rightarrow$ O*, O* $\rightarrow$ OOH*, OOH* $\rightarrow$ O$_2$(g)) was assumed. The Gibbs free energies of the OER intermediates calculated via computational hydrogen electrode method[66] include room temperature corrections, zero point energy (ZPE), and the vibrational enthalpy and entropy contributions (relative to H$_2$(g) and H$_2$O(l)) obtained by means of the harmonic approximation. Combined effect of total energies of adsorption for O2c (O1c) sites were: $\Delta G_{corr.}$ (OH*)= 0.3343 (0.3393) eV, $\Delta G_{corr.}$ (O*)= 0.0145 (0.0005) eV, and $\Delta G_{corr.}$ (OOH*)= 0.3478 (0.3638) eV, respectively. The fully optimized bulk models, reference structures and their respective energies are included as part of the Catalysis-hub.org repository[87].

Acknowledgments:

Author Contributions

655 J.S. conceived the project, synthesized, characterized, performed electrochemical testing of all
656 catalysts, and drafted the manuscript under the supervision of L.A.K and T.F.J. J.S., M.B.S., and
657 A.G. conducted XAS measurements. A.R.Y. and M.R performed part of the catalyst synthesis and
658 electrochemical assessments. J.S., M.B.S, and L.A.K prepared and revised the original drafts of
659 the manuscript. All authors contributed to data analysis, interpretations, and the final version of
660 the manuscript.

Author ORCID

662 Joel Sanchez.: 0000-0001-7723-3345

663 Michaela Burke Stevens: 0000-0003-3584-0600

664 Alessandro Gallo: 0000-0003-4687-8188

665 Mario V. Ramos-Garcés: 0000-0002-7511-9941

666   Jorge L. Colón: 0000-0003-1398-2405

667   Laurie A. King: 0000-0002-0772-2378

668   Michal Bajdich: 0000-0003-1168-8616

669   Thomas F. Jaramillo: 0000-0001-9900-0622

670   **Competing Interests:**

671   The authors declare no competing interests.

672   **Data Availability**

673   All the data needed to support the plots and evaluate the conclusions within this article are present

674   within it, the Supplementary Information, or available from the corresponding author(s) upon

675   request.

676   **Supplementary Information**

677   Supplementary Figs. 1-18, Supplementary Table 1, Supplementary Note 1, and Supplementary

678   References.

679   **References:**

680   1.   Suen, N.-T. *et al.* Electrocatalysis for the oxygen evolution reaction: recent development and future
681   perspectives. *Chem. Soc. Rev.* **46**, 337–365 (2017).

682   2.   Wang, H.-F. & Xu, Q. Materials Design for Rechargeable Metal-Air Batteries. *Matter* **1**, 565–595 (2019).

683   3.   Nitopi, S. *et al.* Progress and Perspectives of Electrochemical CO 2 Reduction on Copper in Aqueous
684   Electrolyte. *Chem. Rev.* **119**, 7610–7672 (2019).

685   4.   Song, F. *et al.* Transition Metal Oxides as Electrocatalysts for the Oxygen Evolution Reaction in Alkaline
686   Solutions: An Application-Inspired Renaissance. *J. Am. Chem. Soc.* **140**, 7748–7759 (2018).

687   5.   Burke, M. S., Enman, L. J., Batchellor, A. S., Zou, S. & Boettcher, S. W. Oxygen Evolution Reaction
688   Electrocatalysis on Transition Metal Oxides and (Oxy)hydroxides: Activity Trends and Design Principles.
689   *Chem. Mater.* **27**, 7549–7558 (2015).

690   6.   Lv, L., Yang, Z., Chen, K., Wang, C. & Xiong, Y. 2D Layered Double Hydroxides for Oxygen Evolution
691   Reaction: From Fundamental Design to Application. *Adv. Energy Mater.* **9**, 1803358 (2019).

692   7.   Shi, Q. *et al.* Metal–organic frameworks-based catalysts for electrochemical oxygen evolution. *Mater.*
693   *Horizons* **6**, 684–702 (2019).

694   8.   Xu, H., Cheng, D., Cao, D. & Zeng, X. C. A universal principle for a rational design of single-atom
695   electrocatalysts. *Nat. Catal.* **1**, 339–348 (2018).

696   9.   Gong, M. & Dai, H. A mini review of NiFe-based materials as highly active oxygen evolution reaction
697   electrocatalysts. *Nano Res.* **8**, 23–39 (2015).

698   10.   Görlin, M. *et al.* Oxygen Evolution Reaction Dynamics, Faradaic Charge Efficiency, and the Active Metal
699   Redox States of Ni–Fe Oxide Water Splitting Electrocatalysts. *J. Am. Chem. Soc.* **138**, 5603–5614 (2016).

700   11.   Batchellor, A. S. & Boettcher, S. W. Pulse-Electrodeposited Ni-Fe (Oxy)hydroxide Oxygen Evolution
701   Electrocatalysts with High Geometric and Intrinsic Activities at Large Mass Loadings. *ACS Catal.* **5**, 6680–
702   6689 (2015).

703   12.   Louie, M. W. & Bell, A. T. An Investigation of Thin-Film Ni–Fe Oxide Catalysts for the Electrochemical
704   Evolution of Oxygen. *J. Am. Chem. Soc.* **135**, 12329–12337 (2013).

705   13.   Trotochaud, L., Young, S. L., Ranney, J. K. & Boettcher, S. W. Nickel–Iron Oxyhydroxide Oxygen-
706   Evolution Electrocatalysts: The Role of Intentional and Incidental Iron Incorporation. *J. Am. Chem. Soc.*
707   **136**, 6744–6753 (2014).

708   14.   Corrigan, D. A. The Catalysis of the Oxygen Evolution Reaction by Iron Impurities in Thin Film Nickel
709   Oxide Electrodes. *J. Electrochem. Soc.* **134**, 377 (1987).

710   15.   Shifa, T. A. & Vomiero, A. Confined Catalysis: Progress and Prospects in Energy Conversion. *Adv. Energy*
711   *Mater.* **9**, 1902307 (2019).

712   16.   Li, H., Xiao, J., Fu, Q. & Bao, X. Confined catalysis under two-dimensional materials. *Proc. Natl. Acad.*
713   *Sci.* **114**, 5930–5934 (2017).

714   17.   Remsing, R. C., McKendry, I. G., Strongin, D. R., Klein, M. L. & Zdilla, M. J. Frustrated Solvation
715   Structures Can Enhance Electron Transfer Rates. *J. Phys. Chem. Lett.* **6**, 4804–4808 (2015).

716   18.   Remsing, R. C. & Klein, M. L. Solvation dynamics in water confined within layered manganese dioxide.
717   *Chem. Phys. Lett.* **683**, 478–482 (2017).

718   19.   Hahn, C. & Jaramillo, T. F. Using Microenvironments to Control Reactivity in CO2 Electrocatalysis. *Joule*
719   **4**, 292–294 (2020).

720   20.   Augustyn, V. & Gogotsi, Y. 2D Materials with Nanoconfined Fluids for Electrochemical Energy Storage.
721   *Joule* **1**, 443–452 (2017).

722   21.   Fleischmann, S., Spencer, M. A. & Augustyn, V. Electrochemical Reactivity under Confinement Enabled by
723   Molecularly Pillared 2D and Layered Materials. *Chem. Mater.* acs.chemmater.0c00648 (2020).
724   doi:10.1021/acs.chemmater.0c00648

725   22.   Gauthier, J. A., Dickens, C. F., Chen, L. D., Doyle, A. D. & Nørskov, J. K. Solvation Effects for Oxygen
726   Evolution Reaction Catalysis on IrO 2 (110). *J. Phys. Chem. C* **121**, 11455–11463 (2017).

727   23.   Doyle, A. D., Montoya, J. H. & Vojvodic, A. Improving Oxygen Electrochemistry through Nanoscopic
728   Confinement. *ChemCatChem* **7**, 738–742 (2015).

729   24.   Doyle, A. D., Bajdich, M. & Vojvodic, A. Theoretical Insights to Bulk Activity Towards Oxygen Evolution
730   in Oxyhydroxides. *Catal. Letters* **147**, 1533–1539 (2017).

731 25. McKendry, I. G. *et al.* Systematic Doping of Cobalt into Layered Manganese Oxide Sheets Substantially
732   Enhances Water Oxidation Catalysis. *Inorg. Chem.* **57**, 557–564 (2018).

733 26. Thenuwara, A. C. *et al.* Intercalation of Cobalt into the Interlayer of Birnessite Improves Oxygen Evolution
734   Catalysis. *ACS Catal.* **6**, 7739–7743 (2016).

735 27. Thenuwara, A. C. *et al.* Copper-Intercalated Birnessite as a Water Oxidation Catalyst. *Langmuir* **31**, 12807–
736   12813 (2015).

737 28. Kang, Q. *et al.* Effect of Interlayer Spacing on the Activity of Layered Manganese Oxide Bilayer Catalysts
738   for the Oxygen Evolution Reaction. *J. Am. Chem. Soc.* **139**, 1863–1870 (2017).

739 29. Luo, Y. *et al.* Two-Dimensional MoS2 Confined Co(OH)2 Electrocatalysts for Hydrogen Evolution in
740   Alkaline Electrolytes. *ACS Nano* **12**, 4565–4573 (2018).

741 30. Chen, Z. *et al.* Interface confined hydrogen evolution reaction in zero valent metal nanoparticles-intercalated
742   molybdenum disulfide. *Nat. Commun.* **8**, 14548 (2017).

743 31. Tang, C. *et al.* Spatially Confined Hybridization of Nanometer-Sized NiFe Hydroxides into Nitrogen-Doped
744   Graphene Frameworks Leading to Superior Oxygen Evolution Reactivity. *Adv. Mater.* **27**, 4516–4522
745   (2015).

746 32. Lei, F. *et al.* Metallic tin quantum sheets confined in graphene toward high-efficiency carbon dioxide
747   electroreduction. *Nat. Commun.* **7**, 12697 (2016).

748 33. Santiago, M. B. *et al.* Layered Inorganic Materials as Redox Agents: Ferrocenium-Intercalated Zirconium
749   Phosphate. *Langmuir* **23**, 7810–7817 (2007).

750 34. Santiago, M. B. *et al.* NADH Electrooxidation Using Bis(1,10-phenanthroline-5,6-dione)(2,2′-
751   bipyridine)ruthenium(II)-Exchanged Zirconium Phosphate Modified Carbon Paste Electrodes.
752   *Electroanalysis* **18**, 559–572 (2006).

753 35. Santiago, M. B. *et al.* Effect of Enzyme and Cofactor Immobilization on the Response of Ethanol Oxidation
754   in Zirconium Phosphate Modified Biosensors. *Electroanalysis* **22**, 1097–1105 (2010).

755 36. Rivera, E. J. *et al.* Vapochromic and vapoluminescent response of materials based on platinum(ii)
756   complexes intercalated into layered zirconium phosphate. *J. Mater. Chem.* **21**, 15899 (2011).

757 37. Rivera, E. J., Figueroa, C., Colón, J. L., Grove, L. & Connick, W. B. Room-temperature emission from
758   platinum(II) complexes intercalated into zirconium phosphate-layered materials. *Inorg. Chem.* **46**, 8569–
759   8576 (2007).

760 38. Rivera, E. J. *et al.* Luminescence Rigidochromism and Redox Chemistry of Pyrazolate-Bridged Binuclear
761   Platinum(II) Diimine Complex Intercalated into Zirconium Phosphate Layers. *Inorg. Chem.* **51**, 2777–2784
762   (2012).

763 39. Casañas-Montes, B. *et al.* Molybdocene dichloride intercalation into zirconium phosphate nanoparticles. *J.*
764   *Organomet. Chem.* **791**, 34–40 (2015).

765 40. González-Villegas, J. *et al.* Poly(ethylene glycol)-modified zirconium phosphate nanoplatelets for improved
766   doxorubicin delivery. *Inorganica Chim. Acta* **468**, 270–279 (2017).

767 41. Díaz, A. *et al.* Nanoencapsulation of insulin into zirconium phosphate for oral delivery applications.
768   *Biomacromolecules* **11**, 2465–2470 (2010).

769 42. Díaz, A. *et al.* Direct intercalation of cisplatin into zirconium phosphate nanoplatelets for potential cancer
770   nanotherapy. *Nanoscale* **5**, 11456 (2013).

771 43. Díaz, A. *et al.* Zirconium phosphate nanoplatelets: a novel platform for drug delivery in cancer therapy.
772   *Chem. Commun.* **48**, 1754 (2012).

773 44. Sanchez, J., Ramos-Garcés, M. V., Narkeviciute, I., Colón, J. L. & Jaramillo, T. F. Transition Metal-
774   Modified Zirconium Phosphate Electrocatalysts for the Oxygen Evolution Reaction. *Catalysts* **7**, 132 (2017).

775 45. Ramos-Garcés, M. V. *et al.* Transition Metal-Modified Exfoliated Zirconium Phosphate as an
776   Electrocatalyst for the Oxygen Evolution Reaction. *ACS Appl. Energy Mater.* **2**, 3561–3567 (2019).

777 46. Ramos-Garcés, M. V. *et al.* Morphology control of metal-modified zirconium phosphate support structures
778   for the oxygen evolution reaction. *Dalt. Trans.* **49**, 3892–3900 (2020).

779 47. V. Ramos-Garcés, M. *et al.* Water Splitting Electrocatalysis within Layered Inorganic Nanomaterials. in
780   *Water Chemistry* (IntechOpen, 2020). doi:10.5772/intechopen.88116

781 48. Alberti, G. & Costantino, U. Recent progress in the intercalation chemistry of layered α-zirconium
782   phosphate and its derivatives, and future perspectives for their use in catalysis. *J. Mol. Catal.* **27**, 235–250
783   (1984).

784 49. Kijima, T. Direct Preparation of θ-Zirconium Phosphate. *Bull. Chem. Soc. Jpn.* **55**, 3031–3032 (1982).

785 50. Kolitsch, U. The crystal structure of wycheproofite, NaAlZr(PO4)2(OH)2 H2O. *Eur. J. Mineral.* **15**, 1029–
786   1034 (2004).

787 51. Rudolf, P. R. & Clearfield, A. X-ray powder structure and Rietveld refinement of the monosodium
788   exchanged monohydrate of .alpha.-zirconium phosphate, Zr(NaPO4)(HPO4).cntdot.H2O. *Inorg. Chem.* **28**,
789   1706–1710 (1989).

790 52. Sun, L. *et al.* The effect of guest molecular architecture and host crystallinity upon the mechanism of the
791   intercalation reaction. *J. Colloid Interface Sci.* **333**, 503–509 (2009).

792 53. Brunet, E., Colón, J. L. & Clearfield, A. *Tailored Organic-Inorganic Materials. Tailored Organic-Inorganic*
793   *Materials* (John Wiley & Sons, Inc, 2015). doi:10.1002/9781118792223

794 54. Burke, M. S., Kast, M. G., Trotochaud, L., Smith, A. M. & Boettcher, S. W. Cobalt–Iron (Oxy)hydroxide
795   Oxygen Evolution Electrocatalysts: The Role of Structure and Composition on Activity, Stability, and
796   Mechanism. *J. Am. Chem. Soc.* **137**, 3638–3648 (2015).

797 55. Kibsgaard, J. & Chorkendorff, I. Considerations for the scaling-up of water splitting catalysts. *Nat. Energy*
798   **4**, 430–433 (2019).

799 56. Han, B. *et al.* Screening Oxide Support Materials for OER Catalysts in Acid. *J. Electrochem. Soc.* **165**,
800   F813–F820 (2018).

801 57. Yi, Y. *et al.* Electrochemical corrosion of a glassy carbon electrode. *Catal. Today* **295**, 32–40 (2017).

802 58. Han, L. *et al.* Synthesis and Performance of Functionalized α -Zirconium Phosphate Modified with
803   Octadecyl Isocyanate. *J. Nanomater.* **2018**, 1–9 (2018).

804 59. Bergerhoff, G. & B. *Crystallographic Databases: Information Content, Software Systems, Scientific*
805   *Applications*. (International Union of Crystallography, 1987).

806   60.   Belsky, A., Hellenbrandt, M., Karen, V. L. & Luksch, P. New developments in the Inorganic Crystal
807   Structure Database (ICSD): accessibility in support of materials research and design. *Acta Crystallogr. Sect.*
808   *B Struct. Sci.* **58**, 364–369 (2002).

809   61.   Baker, J. G. *et al.* The Role of Aluminum in Promoting Ni–Fe–OOH Electrocatalysts for the Oxygen
810   Evolution Reaction. *ACS Appl. Energy Mater.* **2**, 3488–3499 (2019).

811   62.   Burns, R. G. *Mineralogical Applications of Crystal Field Theory*. (Cambridge University Press, 1993).
812   doi:10.1017/CBO9780511524899

813   63.   Zhou, Y. & López, N. The Role of Fe Species on NiOOH in Oxygen Evolution Reactions. *ACS Catal.* **10**,
814   6254–6261 (2020).

815   64.   Liu, Y. *et al.* Electrochemical tuning of olivine-type lithium transition-metal phosphates as efficient water
816   oxidation catalysts. *Energy Environ. Sci.* **8**, 1719–1724 (2015).

817   65.   Friebel, D. *et al.* Identification of Highly Active Fe Sites in (Ni,Fe)OOH for Electrocatalytic Water
818   Splitting. *J. Am. Chem. Soc.* **137**, 1305–1313 (2015).

819   66.   Nørskov, J. K. *et al.* Origin of the Overpotential for Oxygen Reduction at a Fuel-Cell Cathode. *J. Phys.*
820   *Chem. B* **108**, 17886–17892 (2004).

821   67.   Man, I. C. *et al.* Universality in Oxygen Evolution Electrocatalysis on Oxide Surfaces. *ChemCatChem* **3**,
822   1159–1165 (2011).

823   68.   Liao, P., Keith, J. A. & Carter, E. A. Water oxidation on pure and doped hematite (0001) surfaces:
824   Prediction of Co and Ni as effective dopants for electrocatalysis. *J. Am. Chem. Soc.* **134**, 13296–13309
825   (2012).

826   69.   Zaffran, J. *et al.* Influence of Electrolyte Cations on Ni(Fe)OOH Catalyzed Oxygen Evolution Reaction.
827   *Chem. Mater.* **29**, 4761–4767 (2017).

828   70.   Hunter, B. M., Gray, H. B. & Müller, A. M. Earth-Abundant Heterogeneous Water Oxidation Catalysts.
829   *Chem. Rev.* **116**, 14120–14136 (2016).

830   71.   Hunter, B. M. *et al.* Trapping an Iron(VI) Water-Splitting Intermediate in Nonaqueous Media. *Joule* **2**, 747–
831   763 (2018).

832   72.   Li, N. *et al.* Influence of iron doping on tetravalent nickel content in catalytic oxygen evolving films. *Proc.*
833   *Natl. Acad. Sci.* **114**, 1486–1491 (2017).

834   73.   Enman, L. J. *et al.* Operando X-Ray Absorption Spectroscopy Shows Iron Oxidation Is Concurrent with
835   Oxygen Evolution in Cobalt-Iron (Oxy)hydroxide Electrocatalysts. *Angew. Chemie Int. Ed.* **57**, 12840–
836   12844 (2018).

837   74.   Stevens, M. B., Trang, C. D. M., Enman, L. J., Deng, J. & Boettcher, S. W. Reactive Fe-Sites in Ni/Fe
838   (Oxy)hydroxide Are Responsible for Exceptional Oxygen Electrocatalysis Activity. *J. Am. Chem. Soc.* **139**,
839   11361–11364 (2017).

840   75.   van Aken, P. A., Liebscher, B. & Styrsa, V. J. Quantitative determination of iron oxidation states in minerals
841   using Fe L 2,3 -edge electron energy-loss near-edge structure spectroscopy. *Phys. Chem. Miner.* **25**, 323–
842   327 (1998).

843   76.   Thenuwara, A. C. *et al.* Nickel Confined in the Interlayer Region of Birnessite: an Active Electrocatalyst for

844   Water Oxidation. *Angew. Chemie - Int. Ed.* **55**, 10381–10385 (2016).

845   77.   Shan, X. *et al.* Structural water and disordered structure promote aqueous sodium-ion energy storage in
846   sodium-birnessite. *Nat. Commun.* **10**, 1–11 (2019).

847   78.   Amann-Winkel, K. *et al.* X-ray and Neutron Scattering of Water. *Chemical Reviews* **116**, 7570–7589 (2016).

848   79.   Clearfield, A. & Kalnins, J. M. On the mechanism of ion exchange in zirconium phosphates—XIII. *J. Inorg.*
849   *Nucl. Chem.* **38**, 849–852 (1976).

850   80.   Kresse, G. & Furthmüller, J. Efficiency of ab-initio total energy calculations for metals and semiconductors
851   using a plane-wave basis set. *Comput. Mater. Sci.* **6**, 15–50 (1996).

852   81.   Kresse, G. Ab initio molecular dynamics for liquid metals. *J. Non. Cryst. Solids* **192–193**, 222–229 (1995).

853   82.   Kresse, G. & Joubert, D. From ultrasoft pseudopotentials to the projector augmented-wave method. *Phys.*
854   *Rev. B* **59**, 1758–1775 (1999).

855   83.   Perdew, J. P., Burke, K. & Ernzerhof, M. Generalized Gradient Approximation Made Simple. *Phys. Rev.*
856   *Lett.* **77**, 3865–3868 (1996).

857   84.   Dudarev, S. L., Botton, G. A., Savrasov, S. Y., Humphreys, C. J. & Sutton, A. P. Electron-energy-loss
858   spectra and the structural stability of nickel oxide: An LSDA+U study. *Phys. Rev. B* **57**, 1505–1509 (1998).

859   85.   Li, Y.-F. & Selloni, A. Mechanism and Activity of Water Oxidation on Selected Surfaces of Pure and Fe-
860   Doped NiO x. *ACS Catal.* **4**, 1148–1153 (2014).

861   86.   Bajdich, M., García-Mota, M., Vojvodic, A., Nørskov, J. K. & Bell, A. T. Theoretical Investigation of the
862   Activity of Cobalt Oxides for the Electrochemical Oxidation of Water. *J. Am. Chem. Soc.* **135**, 13521–13530
863   (2013).

864   87.   Winther, K. T. *et al.* Catalysis-Hub.org, an open electronic structure database for surface reactions. *Sci. data*
865   **6**, 75 (2019).

866